Concepts relating magnetic interactions, intertwined electronic orders, and strongly correlated superconductivity

J. C. Séamus Davis[a,b,c,d,1] and Dung-Hai Lee[e,f,1]

[a]Department of Physics, Cornell University, Ithaca, NY 14853; [b]Condensed Matter Physics and Material Science Department, Brookhaven National Laboratory, Upton, NY 11973; [c]School of Physics and Astronomy, University of St. Andrews, Fife KY16 9SS, Scotland; [d]Kavli Institute at Cornell for Nanoscale Science, Cornell University, Ithaca, NY 14853; [e]Department of Physics, University of California, Berkeley, CA 94720; and [f]Materials Science Division, Lawrence Berkeley National Laboratory, Berkeley, CA 94720

This contribution is part of the special series of Inaugural Articles by members of the National Academy of Sciences elected in 2010.

Contributed by J. C. Séamus Davis, September 9, 2013 (sent for review July 13, 2013)

Unconventional superconductivity (SC) is said to occur when Cooper pair formation is dominated by repulsive electron–electron interactions, so that the symmetry of the pair wave function is other than an isotropic s-wave. The strong, on-site, repulsive electron–electron interactions that are the proximate cause of such SC are more typically drivers of commensurate magnetism. Indeed, it is the suppression of commensurate antiferromagnetism (AF) that usually allows this type of unconventional superconductivity to emerge. Importantly, however, intervening between these AF and SC phases, intertwined electronic ordered phases (IP) of an unexpected nature are frequently discovered. For this reason, it has been extremely difficult to distinguish the microscopic essence of the correlated superconductivity from the often spectacular phenomenology of the IPs. Here we introduce a model conceptual framework within which to understand the relationship between AF electron–electron interactions, IPs, and correlated SC. We demonstrate its effectiveness in simultaneously explaining the consequences of AF interactions for the copper-based, iron-based, and heavy-fermion superconductors, as well as for their quite distinct IPs.

high-Tc superconductivity | strong correlations | fermiology

Emergence, the coming into being through evolution, is an important concept in modern condensed matter physics (1). Superconductivity is a classic example of emergence in the realm of quantum matter: as the energy scale decreases, the effective electron–electron interactions responsible for Cooper pairing and thus superconductivity evolves from the elementary microscopic Hamiltonian through unanticipated modifications (2). This evolution is why it is so difficult to derive superconductivity (SC) from first principles. Finding the microscopic mechanism of Cooper pairing means discovering the nature of the ultimate effective electron–electron interaction at the lowest energy scales.

In the last three decades, unconventional (3–5) forms of SC have been discovered in many strongly correlated (repulsive electron–electron interaction) systems. These materials fascinate a lay person for their high superconducting transition temperatures and therefore the potential for revolutionary applications in power generation/transmission, transport, information technology, science, and medicine. They intrigue (and challenge) physicists to identify the mechanism of their high pairing-energy scale and because of the many intertwined (6, 7) electronic phases (IPs) that have been discovered in juxtaposition with the unconventional superconductivity. These IPs have been hypothesized to "arise together from one parent state" such that "the various order parameters are intertwined rather than simply competing with each other" (7). The best known and most widely studied examples of such materials include the copper-based (8–11) and iron-based (12–14) high-temperature superconductors, the heavy fermion superconductors (15–17), and the organic superconductors (18). One thing commonly noted in these systems is that SC normally borders antiferromagnetism (AF): in the phase diagram spanned by temperature and a certain control parameter (chemical-doping, pressure, etc.), an SC dome stands adjacent to the AF phase (Fig.1). However, the precise way the two phases are connected varies greatly from system to system.

Another very common observation is the appearance of other ordered phases of electronic matter that intertwine with the SC. These exotic intertwined phases (IPs) occur in the terra incognita between the SC and the AF (Fig. 1, gray). Examples include the charge/spin density wave (19–21) and intra-unit-cell symmetry breaking (21–23) orders in the copper-based superconductors and the nematic order (24, 25) in the iron-based superconductors. A key long-term objective for this field has therefore been to identify a simple framework within which to consider the relationship between the antiferromagnetic interactions, the intertwined electronic orders that appear at its suppression, and the correlated superconductivity.

Because in all of the systems considered here SC emerges from the extinction of AF, it is widely believed that the effective electron–electron interaction triggering the Cooper pairing could be AF in form. In that case, of course, the same argument could apply to the other intertwined electronic phases. These ideas motivate the assertion that AF effective electron–electron interactions may drive both the correlated SC and the other IPs. Until recently, however, there has been little consensus on this issue. One reason is that the experimental evidence for many such intertwined states has only been firmly established in recent years. Another reason is that, although magnetism in proximity to unconventional SC appears universal, the nature of the IPs changes from system to system for reasons that appear mysterious.

In this paper, we therefore explore the plausibility that an AF effective interaction could be the driving force for both the unconventional SC and the intertwined orders in the copper-based, iron-based, and heavy fermion superconductors. [We omit discussion of organic superconductors (26, 27) for the sake of brevity.] Here we will not try to rigorously solve for the ground state under different conditions. Our goal is to ask whether the known IPs are the locally stable mean-field phases when the sole

Significance

This study describes a unified theory explaining the rich ordering phenomena, each associated with a different symmetry breaking, that often accompany high-temperature superconductivity. The essence of this theory is an "antiferromagnetic interaction," the interaction that favors the development of magnetic order where the magnetic moments reverse direction from one crystal unit cell to the next. We apply this theory to explain the superconductivity, as well as all observed accompanying ordering phenomena in the copper-oxide superconductors, the iron-based superconductors, and the heavy fermion superconductors.

Author contributions: J.C.S.D. and D.-H.L. designed research, performed research, analyzed data, and wrote the paper.

The authors declare no conflict of interest.

Freely available online through the PNAS open access option.

[1]To whom correspondence may be addressed. E-mail: dunghai@berkeley.edu and jcdavis@ccmr.cornell.edu.

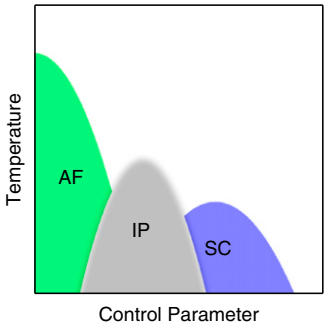

Fig. 1. Schematic phase diagram of unconventional superconductors. Starting from a robust commensurate AF, a control parameter, such as carrier density or pressure, is varied so that the critical temperature T_{AF} of the AF phase diminishes. Eventually, an unconventional SC phase appears at higher values of the control parameter, and its critical temperature T_c is usually dome shaped. The intervening gray region is where the AF phase and the SC phase connect. It is here that the intertwined phases of electronic matter have typically been discovered. The characteristics of the IPs are highly distinctive to each system, as is the precise way (e.g., first order, coexistence, quantum critical) that the AF–SC connection occurs. By contrast, the appearance of unconventional SC phase on suppression of an AF state is virtually universal.

effective electron–electron interaction is AF. We understand that the actual effective interactions may be more complex than this simplest AF form; we deliberately omit these details with the goal of identifying a simple framework within which all of the relevant phenomena can be considered. Two very recent preprints based on a related approach, but focusing only on the copper-oxide superconductors, have been published (28, 29).

Effective Hamiltonian

Thus, we start by studying the assertion that fermiology (the Fermi surface topology) + AF effective electron–electron interaction can generate the known IPs in different types of correlated SC materials. Our effective Hamiltonian is viewed as evolved from the bare Hamiltonian for strong Coulomb interactions, and our strategy is to explore, in different ordering channels, which order dominates as the exchange constants of the effective interactions increase from zero. Under these circumstances, it is the AF interaction that is universal, whereas it is the fermiology that is not. The effective Hamiltonian corresponding to our assertion is

$$H_{eff} = \sum_{\mathbf{k}}{}' \sum_{s} \epsilon(\mathbf{k}) n_s(\mathbf{k}) + \sum_{i,j} J_{ij} \mathbf{S}_i \cdot \mathbf{S}_j. \qquad [1]$$

Here, $\mathbf{k}$ and s are the momentum and spin labels, respectively. $\mathbf{S}_i$ represents the total spin operator in the ith unit cell and is given by $\frac{1}{2}\sum_{\tau,s} c^{\dagger}_{i\tau s} \vec{\sigma}_{ss'} c_{i\tau s}$, where τ labels the degrees of freedom in each unit cell (e.g., orbital, different sites). In addition, in Eq. **1**, $\Sigma'_{\mathbf{k}}$ is a sum restricted to the neighborhood of the Fermi surface (which can have several disconnected pieces), $\epsilon(\mathbf{k})$ is the dispersion of the relevant band in the vicinity of the Fermi surface, and $J_{ij}\mathbf{S}_i \cdot \mathbf{S}_j$ should be understood as an electron–electron scattering term. Although we write it in real space, it should be converted to the band eigen-basis and projected to the neighborhood of the Fermi surface for each different type of system.

Obviously, many simplifying assumptions have already been made here. Note that, aside from the fact that $\Sigma'_{\mathbf{k}}$ restricts states to low single-particle excitation energies, there is no further constraint on the Hilbert space, there is no gauge field, and the particle statistics are the usual Fermi statistics. The only effect of interactions is captured by the J_{ij} term. This simplification asserts that the low energy physics, even nonfermi liquid behavior, can be the result of the AF effective interaction. Therefore, although in the absence of J_{ij} Eq. **1** describes a Fermi liquid, in its presence, the system may behave otherwise precisely because J_{ij} can drive many intertwined instabilities, and strong (critical) fluctuations between these instabilities can then drive non-Fermi liquid behavior. Thus, writing down Eq. **1** is not equivalent to assuming a nearly AF Fermi liquid (30, 31). This statement is particularly true near, for example, the AF quantum critical point where J_{ij} can exhibit a strong dependence on the energy cutoff down to the lowest energy.

Of course, we do understand that many learned readers may question our starting point of Eq. **1**. However, in the search for a simple conceptual framework within which to understand quite different correlated superconductors along with their distinct and complex IPs in multiple material systems (8–17), such a simple starting point can have many advantages.

Copper-Based Superconductors

For the case of the copper-based SCs (8–11), we use a simple one-band model to describe the first term of Eq. **1**; the relevant Fermi surface is shown in Fig. 2*A*. For J_{ij}, we use the simplest nearest neighbor interaction to emulate the AF correlations. The utility of Eq. **1** is validated in part by the Fermi liquid quasi-particle Landau quantization observed by high field quantum oscillation experiments (32, 33); it is theoretically plausible (34) that such Fermi liquid behavior can be regained when the strong magnetic field quenches the relevant fluctuations.

It has been known since the early days of cuprate SC that AF fluctuations can induce d-wave Cooper pairing (35–37). We begin by reproducing what is known. Using the effective Hamiltonian specified above, we obtain (*Methods*) the leading and subleading SC gap functions shown in Fig. 2 *C* and *D*. (The idea to mean-field decouple the magnetic interaction to obtain Cooper pairing originates from refs. 38 and 39.) These two gap functions are approximately described by $\cos k_x - \cos k_y$ and $\cos k_x + \cos k_y$, respectively. This result indicates that the cuprates can have extended s-wave pairing tendency (39) after all. Furthermore, Fig. 2*B* shows how this Fermi surface exhibits eight special hot spots (the red dots) where the AF Brillouin zone (BZ; dashed lines) crosses it. These spots are hypothesized to play a leading role in the interplay of intertwined phases and superconductivity in cuprates (21, 28).

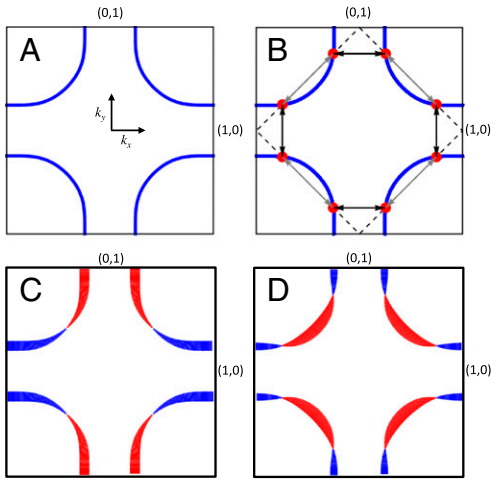

Fig. 2. Fermi surface and unconventional superconducting states of cuprates. (*A*) The cuprate first BZ, within which all of the momentum-space (**k**-space) electronic states of the system are described when not in the AF state. It spans a range $-\pi/a < k_x \le \pi/a$; $-\pi/a < k_y \le \pi/a$, where a is the unit cell dimension. The dimensions of the BZ in *A* are in units of π/a. The model Fermi surface of the cuprates, constructed using a tight-binding single band model with first (t), second (t'), and third (t'') neighbor hopping, where $t'/t = 0.3$ and $t''/t = 0.2$, is shown. (*B*) This Fermi surface exhibits eight special hot spots (the red dots) where the AF BZ (dashed lines) crosses it. They appear to play a leading role in the interplay of intertwined phases and superconductivity (21, 28). The black and gray arrows are the wavevectors of the leading and subleading charge density wave instability. (*C*) The leading spin-singlet superconducting gap function derived from Eq. **1**. The hatch size is proportional to the magnitude and the color indicates the sign (red, –; blue, +). (*D*) The subleading singlet superconducting gap function derived from Eq. **1**. The hatch size is proportional to the magnitude and the color indicates the sign (red, –; blue, +). The gap functions in *C* and *D* are well described by $\cos k_x - \cos k_y$ and $\cos k_x + \cos k_y$, respectively.

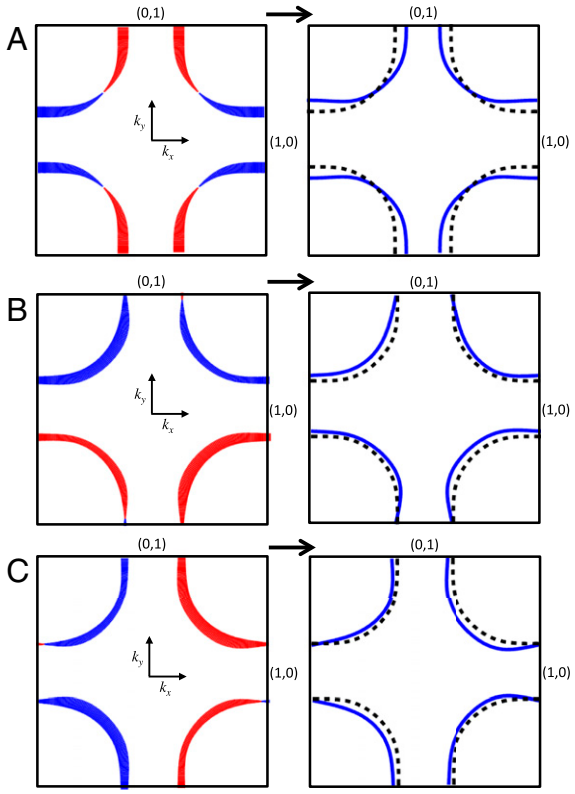

Fig. 3. The $\mathbf{Q} = 0$ intertwined particle-hole instabilities of the cuprates (*Methods*). (*A*) The order parameter of the leading $\mathbf{Q} = 0$ (Pomeranchuk) instability and the associated Fermi surface distortion of cuprates derived from Eq. **1**. Here the hatch size is proportional to the magnitude, and the color indicates the sign (red, –; blue, +), and the dashed line marks the undistorted Fermi surface. This instability breaks the 90° rotation symmetry and leads to nematicity. (*B* and *C*) The order parameter of a degenerate pair of subleading $\mathbf{Q} = 0$ instabilities and the associated Fermi surface distortions. Because the distorted Fermi surfaces are not $\mathbf{k} \leftrightarrow -\mathbf{k}$ symmetric, these instabilities lead to time reversal symmetry breaking.

In the particle–hole interaction channel, Eq. **1** predicts (*Methods*) two types of instabilities: one preserves translation invariance (a $\mathbf{Q} = 0$ instability) and the other (a finite $\mathbf{Q}$ instability) does not. Within our approach, the leading $\mathbf{Q} = 0$ instability is to a nematic state. The order parameter and the associated Fermi surface distortion are shown in Fig. 3*A*. This instability leads to the breaking of the crystal 90° rotation symmetry, such as has been reported within the CuO_2 unit cell (21). The fact that the cuprate Fermi surface has such a tendency to Pomeranchuk distort has been widely discussed (40).

The subleading $\mathbf{Q} = 0$ instability is twofold degenerate. The order parameters and the associated Fermi surface distortions are shown in Fig. 3 *B* and *C*. (Similar instabilities in hexagonal systems were discussed recently in ref. 41.) Because the distorted Fermi surfaces are not $\mathbf{k} \leftrightarrow -\mathbf{k}$ symmetric, these instabilities lead to time reversal symmetry breaking. In Fig. 4*A*, we show the ground state current distribution produced by these order parameters in Fig. 3 *B* and *C*. Depending on the quartic term in the Landau free energy expansion, the order parameters of Fig. 3 *B* and *C* can coexist. In Fig. 4*B*, we show the ground state intra-unit-cell currents associated with the symmetric and antisymmetric combination of the order parameters in Fig. 3 *B* and *C*, respectively. Clearly this subleading time reversal breaking Pomeranchuk instability leads to states with the same broken symmetry as the loop current states proposed in ref. 42 and not inconsistent with reported time reversal symmetry breaking in cuprates (43–45). However, it is important to stress that our $\mathbf{Q} = 0$ instability does not lead to a pseudogap. Moreover, although this instability is subleading here, it is possible that material dependent details omitted in our simple effective action can change that.

The leading $\mathbf{Q} \neq 0$ instability in the particle-hole channel is a charge density wave (CDW) instability [in a recent preprint (28), a related idea was discussed]. The subject of CDW order in cuprate superconductors has a long history. An apparently bidirectional modulated CDW with only short range order is widely observed using spectroscopic imaging scanning tunneling microscopy (21), but it was difficult to be certain these were true bulk phenomena. Therefore, for a long time the only bulk charge density wave order that was firmly established experimentally was the unidirectional charge density wave (stripes) (19) in the La_2BaCuO_4 family of compounds (20). Recently, however, signatures of apparent bidirectional CDW order have been observed by X-ray scattering in bulk $YBa_2Cu_3O_7$ crystals (46–48).

In Fig. 5 *A*–*D*, we present the leading CDW order parameters that are generated by Eq. **1**. Fig. 5 *A*–*D* represents the CDW order parameters whose ordering wavevectors are the four horizontal and vertical black arrows connecting the hot spots in Fig. 2*B*. (The gray arrows are the ordering wavevector of the subleading charge density wave order that we find. This result is different from the result of ref. 28 where the gray arrows are the leading CDW wavevectors, perhaps due to the difference in the details of effective interaction and bandstructure used in the two approaches.) At the quadratic level in a Landau free energy expansion, the order parameters in Fig. 5 *A* and *B* are degenerate with those in panels Fig. 5 *C* and *D*. Depending on the coefficients of the fourth-order terms, they can be either mutually exclusive (which results in a unidirectional CDW) or coexist (which results in a bidirectional CDW). In Fig. 5*E*, we show the energy gap of a bidirectional CDW that corresponds to the out-of-phase coexistence of the order parameters in Fig. 5 *A*–*D* (48).

Finally, the fact that there are both strong nematic (Fig. 3*A*) and CDW (Fig. 5 *A*–*D*) susceptibilities implies that, in the presence of disorder, which can serve as localized external ordering fields, locally nematic and CDW ordering can be induced to coexist. This statement is consistent with the scanning tunnelling microscopy (STM) experiments (21). Such short-range disordered induced ordering can exist even when in the clean limit the system is not yet long-range ordered.

Obviously there is another key issue requiring discussion here: the pseudogap of the cuprates. This unexplained gap to single-electron excitations is anisotropic in $\mathbf{k}$-space and appears at $T^* \gg T_c$ for underdoped cuprates (4, 8, 9, 11, 49). We hypothesize that the consequences of an effective Hamiltonian as described in Eq. **1** could also account for such a pseudogap. The various instabilities

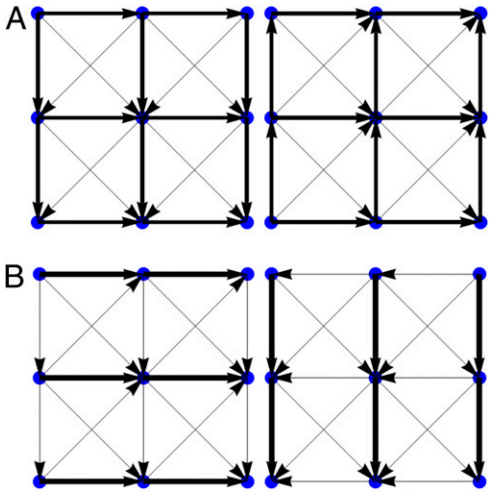

Fig. 4. The ground state current of the T-breaking $\mathbf{Q} = 0$ particle-hole instabilities in the cuprates. (*A*) The ground state current distribution associated with the order parameters in Fig. 3 *B* and *C*. (*B*) The ground state current distribution produced by the symmetric and antisymmetric linear combination of the order parameters in Fig. 3 *B* and *C*. In *A* and *B*, the thickness of the arrow is proportional to the magnitude of the current.

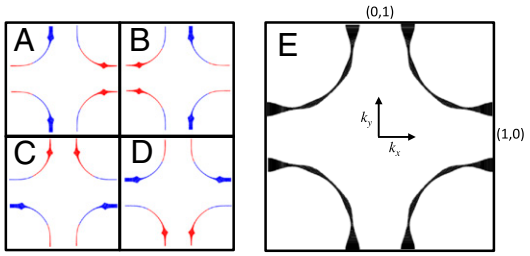

Fig. 5. The leading intertwined $\mathbf{Q} \neq 0$ particle-hole instabilities of the cuprates (*Methods*). The ordering wavevector is $(\pm\delta, 0)$ in *A* and *B* and $(0, \pm\delta)$ in *C* and *D*. The black arrows in Fig. 2*B* are approximately the ordering wavevectors. (*E*) The energy gap of CDW produced by the equal amplitude superposition of the charge density wave depicted in *A*–*D*. The phase of the superposition is taken to be +, +, −, −, and hence corresponds to a d-wave symmetry. (The energy gap associated with the +, +, +, + superposition of *A*–*D* is similar.) The charge density wave gap plotted in *E* is defined as the minimum energy gap of the mean-field Hamiltonian in *Methods* along the momentum cut normal to the Fermi surface but within the energy thin shell. The smallness of this combined order parameter near the nodes can give rise to the effect of Fermi arcs.

(except those at $\mathbf{Q} = 0$) discussed here can all gap out, at least partially, the single-electron excitation spectrum. However, due to the intertwining of these instabilities, the order parameter may fluctuate from one type to another. This fluctuation would prevent the system from becoming long range ordered without eliminating the actual pseudogap for the single-electron excitations.

Thus, we consider the order parameters of different intertwined orders to form a multicomponent supervector. The magnitude of the supervector is then responsible for the single-particle gap. The direction of the supervector is the soft degree of freedom, which ultimately determines the long ranged order of the system. However, although this direction fluctuates, the single-electron excitation spectrum remains gapped. In our case, when the gap is partial, the low energy excitations include both the directional fluctuations of the supervector and the remaining gapless single particle excitations. Of course because of the coupling with the collective excitations, these single-particle excitations can have unusual, e.g., non-Fermi liquid, properties.

Now it remains to show with a supervector formed using the AF, SC, and CDW order parameters that there is a pseudogap in the single electron excitation spectrum, no matter where the supervector points. The results are shown in Fig. 6. In Fig. 6*A*, the supervector points in the AF direction. This supervector is shown by the red arrow on the order parameter sphere on the right. Such an order has the biggest effect at the hot spots (Fig. 2*B*) where the gap is maximal (Fig. 6*A*, *Left*). Here and in other panels, a vanishing single-particle gap at any point on the Fermi surface means that, along the normal direction, there remains Fermi crossing, i.e., the Fermi surface has either moved or reconstructed. The supervector in Fig. 6*B* points in the SC direction. The gap spectrum shown on the left is the familiar d-wave gap. In Fig. 6*C*, the supervector points in the CDW direction. The energy gap spectrum on the left shows a nodal feature. The supervector in Fig. 6*D* lies in the plane spanned by the SC and the CDW but directionally between the two. Finally, in Fig. 6*E*, the supervector points in a generic direction. Obviously in reality, different components of the supervector do not have to have the same norm so that the fluctuations of the supervector actually occur on a spheroid; hence, there is no enlarged symmetry. We hope this figure makes the heuristic case that a pseudogap can also be a consequence of the effective interaction in Eq. **1**, when the effects of fluctuating intertwined order parameters are dominant. Many of the anomalous physical properties in the pseudogap state could then be attributed to orientational fluctuations of this intertwined supervector.

Iron-Based Superconductors

Next we carry out the equivalent exercise for the iron-based superconductors (12–14). The first term of Eq. **1** is studied here using a five-band tight-binding model with the Fermi surface shown in Fig. 7*A*. The blue and red lines mark the hole and electron Fermi surfaces, respectively. To simulate the magnetic correlation in iron-based superconductors, we include both the first (J_1) and second (J_2) neighbor interaction in J_{ij}. (A similar Hamiltonian, with a doped Mott insulator basis, was proposed in ref. 50, 51.) This effective interaction has been derived from the functional renormalization group calculation (52). Phenomenologically, there is mounting evidence that the magnetic correlations in the iron-based materials are not due to Fermi surface nesting (53). It is then more appropriate to view the second term in Eq. **1** as being generated by excitations over the entire bandwidth. The essential difference from a Mott insulator here is the absence of a charge gap. Therefore, the generation of the effective magnetic interactions is more gradual. Using these inputs for $J_2/J_1 \geq 0.7$, we find (*Methods*) the leading and subleading SC order parameter shown in Fig. 7 *B* and *C*, respectively. The leading gap function has the $S_{\pm}$ symmetry (54) and the subleading one has $d_{x^2-y^2}$ symmetry (13, 14).

In the particle-hole interaction channel, we find that (*Methods*) the iron-based superconductors also have strong $\mathbf{Q} = 0$ instabilities. In Fig. 8 *A* and *B*, we show the leading and subleading Fermi surface distortions that we determine from Eq. **1** when the distortion amplitude is small. Here the undistorted Fermi surface is shown using dashed lines. This result agrees with the functional renormalization group findings (52). The leading Fermi surface distortion preserves the point group symmetry of the crystal. Note that because both electron and hole pockets expand (or shrink), it preserves the total charge density. (We note that a large amplitude distortion of this type can drive the system to undergo a semimetal to insulator transition.) The subleading $\mathbf{Q} = 0$ instability breaks the 90° rotation symmetry. Although it is subleading at the quadratic level of the Landau free energy expansion, it can become leading once the cubic coupling with the (strong) AF fluctuation is taken into account [note that the AF order in the iron-based materials also

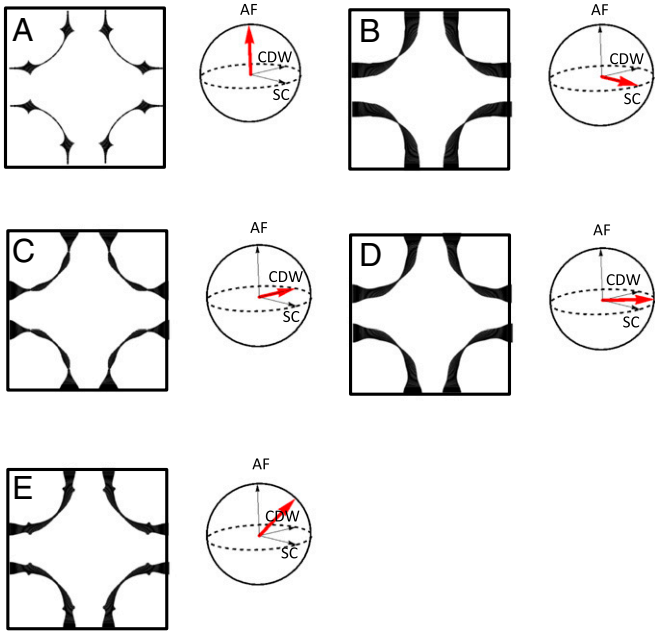

Fig. 6. Intertwined instabilities and the cuprate pseudogap. We represent the three instabilities contained in Eq. **1** (AF, SC, and CDW) using a supervector representing the combination of the three order parameters. The admixture of AF, SC, and CDW phases can then be indicated by using the location of the supervector on a sphere. In each panel from *A* to *E*, the direction of the supervector is shown as the red arrow on the order parameter sphere on the right of the same panel. The gap shown on the left of each panel is the minimum energy gap of the mean-field Hamiltonian in *Methods* along the momentum cut normal to the Fermi surface but within the energy thin shell. The size of the hatch is proportional to the value of the single particle energy gap.

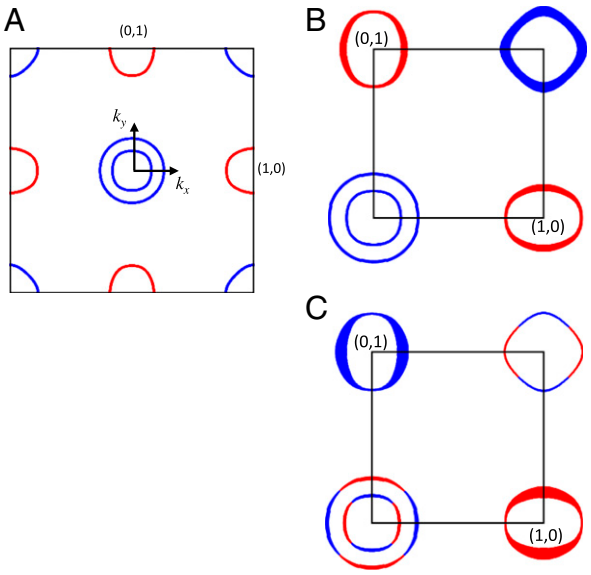

Fig. 7. Model Fermi surface and superconducting states of iron pnictides. (*A*) The pnictide-first BZ when not in the AF state. It spans a range $-\pi/a < k_x \le k_x/a; -\pi/a < k_y \le \pi/a$, where a is the dimension of a unit cell containing only one Fe atom (we neglect the effects on unit cell definition of the out of plane As atoms). Our model Fermi surface of iron-pnictides using a five-band tight-binding model is shown as five closed contours: two red (outline the electron pocket) and three blue (outline the hole pocket). (*B*) The leading spin singlet superconducting gap function derived from Eq. **1**. The symmetry is $S_{\pm}$. The hatch size is proportional to the magnitude, and the color indicates the sign (red, −; blue, +). (*C*) The subleading singlet superconducting gap function derived from Eq. **1**. The symmetry is $d_{x^2-y^2}$. The hatch size is proportional to the magnitude, and the color indicates the sign (red, −; blue, +). The results in *B* and *C* are obtained using $J_2/J_1 = \tan 0.3\pi$.

breaks the 90° rotation symmetry (55)]. In Fig. 8*C*, we show the effect of the symmetry breaking distortion we find on the orbital occupation $n_{xz}(\mathbf{k}) - n_{yz}(\mathbf{k})$. The fact that one needs magnetic fluctuations to stabilize the C_4-breaking Fermi surface distortion is consistent with the arguments presented previously (12, 56, 57). Thus, the result in Fig. 8 *B* and *C* can explain the ubiquitous nematic ordering found in the iron-based superconductors (24, 25). It also accounts for the photoemission observation of the substantial difference in the d_{xz} and d_{yz} orbital occupation in the nematic-distorted state (58).

Within our approach of Eq. **1**, iron-pnictides show a very weak $\mathbf{Q} \neq 0$ CDW instability. The ordering wavevector of the leading CDW is approximately (π, π). However, due to the poor overlaps between the Fermi surfaces on the (π, π) displacement and the fact that (π, π) only approximately connects electron with electron or hole with hole pockets, a weak CDW will not gap out the Fermi surfaces. Therefore, we will not devote more space to consideration of the CDW instability in pnictides.

Heavy Fermion Superconductors

Finally, we use this same conceptual framework to consider the canonical heavy fermion superconductor $CeCoIn_5$. The band structure we used for this material is the one given in ref. 59. The tight-binding model consists of two orbitals per unit cell: the Wannier orbitals associated with the light and heavy bands, respectively. The Fermi surface is shown in Fig. 9*A*. The J_{ij} we use to emulate the AF correlation in $CeCoIn_5$ is the simple nearest neighbor interaction. With these inputs, we determine from Eq. **1** the leading and subleading SC order parameter; the results are shown in Fig. 9 *B* and *C*. The leading superconducting gap function, with $d_{x^2-y^2}$ symmetry (*Methods*), is in excellent agreement with that recently determined by the STM quasiparticle interference spectroscopy (59). The reason that the SC gap primarily opens on the large Fermi surface centered at (π, π) is because the hot spots associated with the AF scattering all reside on that Fermi surface. This fact is shown in Fig. 9*D*. Like the cuprates, the subleading SC gap function has extended s-wave symmetry.

In the particle-hole channel, our general approach in Eq. **1** also predicts that $CeCoIn_5$ has $\mathbf{Q} = 0$ and $\mathbf{Q} \neq 0$ instabilities (*Methods*). The order parameter and the Fermi surface distortion associated with the leading $\mathbf{Q} = 0$ instability is shown in Fig. 10*A*. This distortion breaks the crystal 90° rotation symmetry and leads to nematicity. It is very interesting that, like the cuprates, the subleading $\mathbf{Q} = 0$ instability is also to a degenerate pair of time reversal symmetry breaking states. The order parameter and the distorted Fermi surfaces are shown in Fig. 10 *B* and *C*. The obvious similarity between the $\mathbf{Q} = 0$ instabilities in the heavy fermions and the cuprates is quite striking.

The order parameter of the leading (weak) $\mathbf{Q} \neq 0$ charge density wave instability is shown in Fig. 11 *A*–*D*. The energy gap produced by the in-phase coexistence of the order parameters in Fig. 11 *A* and *B* with those in Fig. 11 *C* and *D* is shown in Fig. 11*E*. Experimental searches of the signatures of these instabilities are under way.

Searching for instabilities intertwined with superconductivity in heavy fermion compounds now seems an important future direction. However, one must bear in mind that the equivalent chemical pressure places $CeCoIn_5$ near the optimal pressure, where the SC transition temperature is the highest. The intertwined instabilities tend to occur near the junction between AF and SC. Therefore, unless negative pressure can somehow be applied, they can remain out of reach for $CeCoIn_5$. A better system for realizing intertwined instabilities is $CeRhIn_5$ which is AF at ambient pressure.

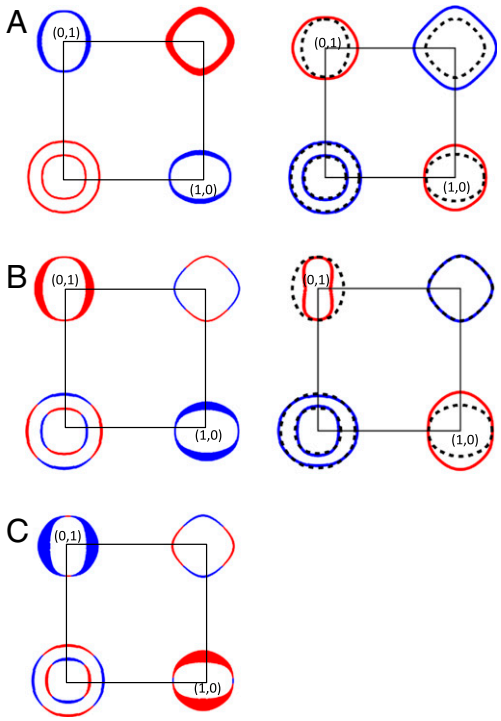

Fig. 8. Leading intertwined instabilities of iron-pnictides. (*A*) The leading $\mathbf{Q} = 0$ instability and the associated Fermi surface distortions in the iron-based superconductors derived from Eq. **1**. The hatch size is proportional to the magnitude, and the color indicates sign (red, −; blue, +). The dashed lines mark the undistorted Fermi surface. The area of both electron and hole pockets expand (or shrink) so that the total charge density is kept constant. This distortion does not break any symmetry and hence is difficult to pin down. (*B*) The subleading $\mathbf{Q} = 0$ instability and the associated Fermi surface distortion derived from Eq. **1**. This distortion breaks the 90° rotation symmetry and couples to the stripe-like unidirectional AF correlation strongly. Although the instability in *B* is subleading at the quadratic level of the Landau free energy expansion, it can become leading once the cubic coupling with the AF order parameter is taken into account. (*C*) The effect of the Fermi surface distortion in *B* on the orbital occupation $n_{xz}(\mathbf{k}) - n_{yz}(\mathbf{k})$.

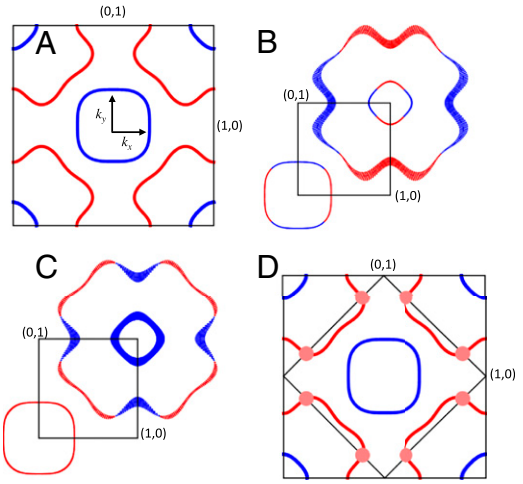

Fig. 9. Fermi surface and unconventional superconducting states of the heavy fermion compound $CeCoIn_5$. (*A*) The first BZ and Fermi surface associated with a two-band band structure in ref. 58. The BZ spans a range $-\pi/a < k_x \le \pi/a$; $-\pi/a < k_y \le \pi/a$, where a is the dimension of a unit cell. The leading (*B*) and subleading (*C*) spin singlet SC gap functions. The leading gap function has $d_{x^2-y^2}$ symmetry and the subleading one has extended S symmetry. In *B* and *C*, the hatch size is proportional to the magnitude of the gap, and the color indicates the sign (red, –; blue, +). (*D*) The Fermi surface and hot spots (the pink dots) of $CeCoIn_5$.

By carefully studying the pressure–temperature phase diagram, one might be able to find similar phenomena as in underdoped cuprates. If so, this will give additional support for applicability of the simple theory envisioned in Eq. **1**.

Conclusion

From the above studies, using the simple concept of a controlling influence of AF electron–electron interactions, it seems fair to say that the low-energy effective Hamiltonian given by Eq. **1** can be very useful in achieving an elementary understanding of the SC and the intertwined instabilities in several canonical classes of unconventional superconductors. Specifically we note that these studies demonstrate why, although superconductivity is universal, the nature of the Fermi surface distortion and/or the density wave instabilities depends so much on the details of the fermiology. Such dependence is the reason why the intertwined electronic ordered states in correlated SC compounds are so strongly material dependent. Moreover, due to these distinct intertwined orders, Eq. **1** does not describe a "nearly antiferromagnetic Fermi liquid." Thus, our approach indicates that many of the anomalous properties of the cuprates and the pnictides may be due to the fluctuations of the order parameter among the relevant intertwined orders, whereas the severity of these fluctuations can be material dependent. We understand that the point of view presented here is simplified. However, with a goal of identifying concepts that can simply relate strong AF electron–electron interactions, intertwined electronic ordered phases, and strongly correlated SC in distinct material types, this is perhaps a good thing. We hope that the approach presented here can help to distill the essence of the unconventional pairing mechanism from the impressive phenomenology of the IPs in present and future strongly correlated high temperature superconductors.

Methods

We used the following procedures to determine the favored competing orders from the effective Hamiltonian, starting with

$$H_{\text{eff}} = \sum_{\mathbf{k}}{}' \sum_{s} \epsilon(\mathbf{k}) n_s(\mathbf{k}) + \sum_{i,j} J_{ij} \vec{S}_i \cdot \vec{S}_j, \qquad [2]$$

where $n_s(\mathbf{k}) = \psi^\dagger_{\mathbf{k},s}\psi_{\mathbf{k},s}$, and $\psi^\dagger_{\mathbf{k},s}$ creates an electron in the single-particle eigenstate at momentum $\mathbf{k}$ with spin s. As mentioned in the text, $\Sigma_{\mathbf{k}}$ restricts the sum to single particle eigenstates whose energy is within a thin shell from the Fermi energy.

First, we reexpress the second term in terms of the band eigen basis:

$$\sum_{i,j} J_{ij} \vec{S}_i \cdot \vec{S}_j = \frac{1}{A} \sum_{\mathbf{k},\mathbf{p},\mathbf{q}} \sum_{s_{1,2,3,4}} V_{\mathbf{q}}(\mathbf{k};\mathbf{p}) \psi^\dagger_{\mathbf{k}+\mathbf{q},s_1} \vec{\sigma}_{s_1,s_2} \psi_{\mathbf{k},s_2} \cdot \psi^\dagger_{\mathbf{p}-\mathbf{q},s_3} \vec{\sigma}_{s_3,s_4} \psi_{\mathbf{p},s_4}, \qquad [3]$$

where

$$V_{\mathbf{q}}(\mathbf{k};\mathbf{p}) = J(\mathbf{q}) \left\{ \phi^*_{\alpha(\mathbf{k}+\mathbf{q})}(\mathbf{k}+\mathbf{q}) \cdot \phi_{\alpha(\mathbf{k})}(\mathbf{k}) \right\} \times \left\{ \phi^*_{\alpha(\mathbf{p}-\mathbf{q})}(\mathbf{p}-\mathbf{q}) \cdot \phi_{\alpha(\mathbf{p})}(\mathbf{p}) \right\}.$$

Here, A is the total area, ϕ is the band eigen wavefunctions in the orbital basis, and $J(\mathbf{q})$ is the Fourier transform of J_{ij}. For the copper-based, iron-based, and heavy fermion superconductors, $J(\mathbf{q})$ is taken to be an overall coupling strength J_{eff} times the following form factors:

$$\begin{array}{l} \cos k_x + \cos k_y (\text{copper} - \text{based}) \\ \cos\theta(\cos k_x + \cos\, k_y) + \sin\theta(2\, \cos k_x \cos k_y)(\text{iron} - \text{based}) \\ \cos k_x + \cos k_y (\text{heavy} - \text{fermion}). \end{array} \qquad [4]$$

J_{eff} is a renormalized coupling strength that is unknown a priori. The result for the iron-based superconductors were generated with $\theta = 0.3\pi$. In $V_{\mathbf{q}}(\mathbf{k};\mathbf{p})$, the band index, e.g., $\alpha(\mathbf{k}+\mathbf{q})$, is defined to be the index of the band that is closest to the Fermi energy at momentum $\mathbf{k}+\mathbf{q}$. If the corresponding single particle state has energy beyond the energy shell, ϕ is set to zero. In Eq. **4**, ϕ is unity, a two-component vector, and a five-component vector for the cuprates, $CeCoIn_5$, and pnictides, respectively. For $CeCoIn_5$, if one decides to include the magnetic interaction between the f electrons only, one needs to replace $\phi^*_{\alpha(\mathbf{p})}(\mathbf{p}) \cdot \phi_{\alpha(\mathbf{q})}(\mathbf{q})$ in Eq. **4** by $\phi^*_{2,\alpha(\mathbf{p})}(\mathbf{p})\phi_{2,\alpha(\mathbf{q})}(\mathbf{q})$, where 2 labels the f electron Wannier orbitals. The results for $CeCoIn_5$ remain qualitatively unchanged using either formula.

The next step is to decouple Eq. **3** in the particle-particle (for Cooper pairing) and particle-hole (for charge and spin density wave and Pomeranchuk distortion). The first-instability-mode analysis described here allows us to determine the functional form of the order parameter. However, it does not fix the overall magnitude. Once the functional form is determined, we use the mean-field Hamiltonians described here to determine the energy gaps, Fermi surface distortions, etc. The overall magnitude of the order

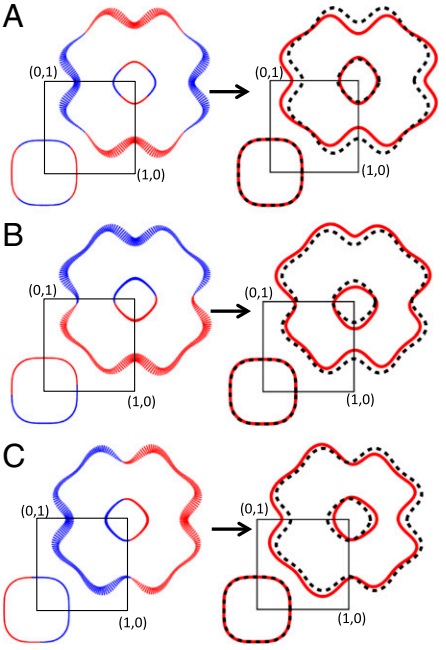

Fig. 10. The intertwined $\mathbf{Q} = 0$ particle-hole Instabilities of $CeCoIn_5$. (*A*) The leading Pomeranchuk instability and the associated Fermi surface distortion. The hatch size is proportional to the magnitude of the order parameter, and the color indicates the sign (red, –; blue, +). The dashed line marks the undistorted Fermi surface. This Fermi surface distortion leads to the breaking of the 90° rotation symmetry. (*B* and *C*) The degenerate pair of subleading Pomeranchuk instabilities and their Fermi surface distortions. In both panels, the distorted Fermi surfaces do not respect the $\mathbf{k} \leftrightarrow -\mathbf{k}$ symmetry. Consequently time reversal symmetry is broken.

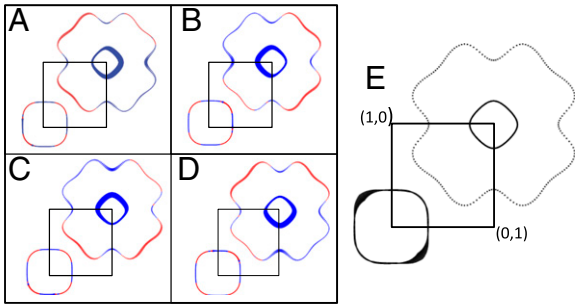

Fig. 11. The leading intertwined $\mathbf{Q} \neq 0$ particle-hole Instabilities of $CeCoIn_5$. (*A–D*) The leading charge density wave order parameter. (*A* and *B*) The ordering wavevectors are $\pm(0.56\pi,0.26\pi)$. (*C* and *D*) The ordering wavevectors are $\pm(0.26\pi,0.56\pi)$. (*E*) The energy gap produced by the in-phase coexistence of order parameters in *A–D*. The hatch size is proportional to the magnitude, and the color indicates the sign (red, −; black and blue, +).

parameter is chosen to yield approximately the same maximal energy gap when each order parameter exists alone. The purpose is to convey the qualitative features not to make quantitative comparative predictions.

Cooper Pairing. In the particle-particle channel, we focused on the spin singlet Cooper pairing. This restriction leads to the following factorization of Eq. **3**:

$$H_{\mathrm{MF}} = \sum_{\mathbf{k}}{}' \sum_{s} \epsilon(\mathbf{k}) n_s(\mathbf{k}) + \frac{3}{A} \sum_{\mathbf{p},\mathbf{k}} \sum_{a,b} V_{sc}(\mathbf{p};\mathbf{k}) \times \left\{ \psi^{+}_{-\mathbf{k},a} \psi^{+}_{\mathbf{k},b} \Delta(\mathbf{p}) \epsilon_{ab} + \Delta^{*}(\mathbf{k}) \epsilon_{ba} \psi_{\mathbf{p},a} \psi_{-\mathbf{p},b} + \Delta^{*}(\mathbf{k}) \Delta(\mathbf{p}) \epsilon^{2}_{ab} \right\}. \quad [5]$$

Here a and b label the spin and $\epsilon_{\uparrow\downarrow} = -\epsilon_{\downarrow\uparrow} = 1$ and $\epsilon_{\uparrow\uparrow} = \epsilon_{\downarrow\downarrow} = 0$. In Eq. **5**

$$V_{sc}(\mathbf{p};\mathbf{k}) = J(\mathbf{p}-\mathbf{k}) \left(\phi^{*}_{\alpha(\mathbf{k})}(-\mathbf{k}) \cdot \phi_{\alpha(\mathbf{p})}(-\mathbf{p}) \right) \times \left(\phi^{*}_{\alpha(\mathbf{k})}(\mathbf{k}) \cdot \phi_{\alpha(\mathbf{p})}(\mathbf{p}) \right). \quad [6]$$

We then integrate out the electrons and keep up to the quadratic terms in Δ's. The result is the following free energy form

$$\frac{1}{A} \sum{}'_{\mathbf{k},\mathbf{p}} \Delta(\mathbf{p}) K_T(\mathbf{p};\mathbf{k}) \Delta^{*}(\mathbf{k}), \quad [7]$$

where

$$K_T(\mathbf{p};\mathbf{k}) = 6V_{sc}(\mathbf{p};\mathbf{k}) - 36 \int \frac{d^2q}{(2\pi)^2} V_{sc}(\mathbf{p};\mathbf{q}) \chi_T(\mathbf{q}) V_{sc}(\mathbf{q};\mathbf{k}), \quad [8]$$

where the temperature (T)-dependent free fermion pair susceptibility is given by

$$\chi_T(\mathbf{k}) \propto \frac{1 - 2f(\epsilon(\mathbf{k}))}{\epsilon(\mathbf{k})}. \quad [9]$$

Here the proportionality constant is unimportant for our purposes because it can be absorbed into the unknown J_{eff} (see below).

The leading (subleading) gap functions are the eigenfunctions of $M_T(\mathbf{q};\mathbf{k}) = \chi_T(\mathbf{q}) V_{sc}(\mathbf{q};\mathbf{k})$ with the largest (second largest) eigenvalue. (The proportionality constant in χ_T changes all eigenvalues by the same multiplicative constant but not the eigenfunctions.) These eigenfunctions are the order parameters that will first (second) become unstable as J_{eff} increases (at a temperature T much less than the thickness of the energy shell). These eigenfunctions are obtained numerically after discretizing the momentum space enclosed by the energy shell [under such discretization, $M_T(\mathbf{q},\mathbf{k})$ becomes a matrix]. We diagonalize the M_T matrix and then average the eigenfunctions along the direction perpendicular to the Fermi surface. This procedure leads to the results presented in the text.

CDW and Pomeranchuk Instability. CDW and Pomeranchuk instability occurs in the spin singlet particle-hole channel. Decoupling Eq. **3** in this channel leads to the following mean-field Hamiltonian:

$$H_{\mathrm{MF}} = \sum_{\mathbf{k}}{}' \sum_{s} \epsilon(\mathbf{k}) n_s(\mathbf{k}) - \frac{3}{A} \sum_{\mathbf{k},\mathbf{p},\mathbf{Q}} V_{cdw}(\mathbf{p};\mathbf{k}) \times \left\{ \Delta_{\mathbf{Q}}(\mathbf{p}) \psi^{\dagger}_{\mathbf{k},a} \psi_{\mathbf{k}+\mathbf{Q},a} + \psi^{\dagger}_{\mathbf{p}+\mathbf{Q},a} \psi_{\mathbf{p},a} \Delta^{*}_{\mathbf{Q}}(\mathbf{k}) - 2\Delta_{\mathbf{Q}}(\mathbf{p}) \Delta^{*}_{\mathbf{Q}}(\mathbf{k}) \right\}. \quad [10]$$

Here

$$V_{cdw}(\mathbf{p};\mathbf{k}) = J(\mathbf{p}-\mathbf{k}) \left(\phi^{*}_{\alpha(\mathbf{p}+\mathbf{Q})}(\mathbf{p}+\mathbf{Q}) \cdot \phi_{\alpha(\mathbf{k}+\mathbf{Q})}(\mathbf{k}+\mathbf{Q}) \right) \times \left(\phi^{*}_{\alpha(\mathbf{k})}(\mathbf{k}) \cdot \phi_{\alpha(\mathbf{p})}(\mathbf{p}) \right). \quad [11]$$

Again, we integrate out the fermions to arrive at the following quadratic free energy form:

$$\frac{1}{A} \sum_{\mathbf{k},\mathbf{p},\mathbf{Q}} \Delta_{\mathbf{Q}}(\mathbf{p}) \tilde{K}_{\mathbf{Q},T}(\mathbf{p};\mathbf{k}) \Delta^{*}_{\mathbf{Q}}(\mathbf{k}), \quad [12]$$

where

$$\tilde{K}_{\mathbf{Q},T}(\mathbf{p};\mathbf{k}) = 6V_{cdw}(\mathbf{k};\mathbf{p}) - 9 \int \frac{d^2q}{(2\pi)^2} V_{cdw}(\mathbf{p};\mathbf{q}) \tilde{\chi}_{\mathbf{Q},T}(\mathbf{q}) V_{cdw}(\mathbf{q};\mathbf{k}). \quad [13]$$

Here the free fermion particle-hole susceptibility is given by

$$\tilde{\chi}_{\mathbf{Q},T}(\mathbf{q}) \propto \frac{f(\epsilon(\mathbf{q}+\mathbf{Q})) - f(\epsilon(\mathbf{q}))}{\epsilon(\mathbf{q}) - \epsilon(\mathbf{q}+\mathbf{Q})}. \quad [14]$$

The leading order parameter is the eigenfunction of $\tilde{M}_{\mathbf{Q},T}(\mathbf{q},\mathbf{k}) = \tilde{\chi}_{\mathbf{Q},T}(\mathbf{q}) V_{cdw}(\mathbf{q};\mathbf{k})$ with the largest eigenvalue. Here we have to search both the ordering wavevector $\mathbf{Q}$ as well as the leading form factor. This task is again achieved numerically after discretizing the momentum space within the energy shell and diagonalizing the resulting matrix $\tilde{M}_{\mathbf{Q},T}$. As before, we perform an average of the eigenvector along the direction perpendicular to the Fermi surface, which leads to the results presented in the text.

The Pomerahnchuk distortion is determined as the leading order parameter in the $\mathbf{Q} \to 0$ limit of $M_{\mathbf{Q},T}$. In our calculation, we always find both $\mathbf{Q} = 0$ and $\mathbf{Q} \neq 0$ instabilities.

Spin Density Wave. A spin density wave is a spin triplet particle-hole instability. Decoupling Eq. **3** in this channel leads to the following mean-field Hamiltonian:

$$H_{\mathrm{MF}} = \sum_{\mathbf{k}}{}' \sum_{s} \epsilon(\mathbf{k}) n_s(\mathbf{k}) + \frac{1}{A} \sum_{\mathbf{p},\mathbf{k},\mathbf{Q}} V_{sdw}(\mathbf{p};\mathbf{k}) \times \left\{ \mathbf{m}_{\mathbf{Q}}(\mathbf{p}) \cdot \psi^{\dagger}_{\mathbf{k},c} \vec{\sigma}_{cd} \psi_{\mathbf{k}+\mathbf{Q},d} + \mathbf{m}^{*}_{\mathbf{Q}}(\mathbf{k}) \cdot \psi^{\dagger}_{\mathbf{p}+\mathbf{Q},a} \vec{\sigma}_{ab} \psi_{\mathbf{p},b} - \mathbf{m}_{\mathbf{Q}}(\mathbf{p}) \cdot \mathbf{m}^{*}_{\mathbf{Q}}(\mathbf{k}) \right\}, \quad [15]$$

where

$$V_{sdw}(\mathbf{p};\mathbf{k}) = J(\mathbf{Q}) \left(\phi^{*}_{\alpha(\mathbf{p}+\mathbf{Q})}(\mathbf{p}+\mathbf{Q}) \cdot \phi_{\alpha(\mathbf{p})}(\mathbf{p}) \right) \times \left(\phi^{*}_{\alpha(\mathbf{k})}(\mathbf{k}) \cdot \phi_{\alpha(\mathbf{k}+\mathbf{Q})}(\mathbf{k}+\mathbf{Q}) \right) + \frac{1}{2} J(\mathbf{p}-\mathbf{k}) \times \left(\phi^{*}_{\alpha(\mathbf{p}+\mathbf{Q})}(\mathbf{p}+\mathbf{Q}) \cdot \phi_{\alpha(\mathbf{k}+\mathbf{Q})}(\mathbf{k}+\mathbf{Q}) \right) \times \left(\phi^{*}_{\alpha(\mathbf{k})}(\mathbf{k}) \cdot \phi_{\alpha(\mathbf{p})}(\mathbf{p}) \right). \quad [16]$$

Like before, we integrate out the fermions. The resulting quadratic free energy form reads to

$$\frac{1}{A} \sum_{\mathbf{k},\mathbf{p}} K_{sdw,\mathbf{Q},T}(\mathbf{p};\mathbf{k}) \mathbf{m}_{\mathbf{Q}}(\mathbf{p}) \cdot \mathbf{m}^{*}_{\mathbf{Q}}(\mathbf{k}), \quad [17]$$

where

$$K_{sdw,\mathbf{Q},T}(\mathbf{p};\mathbf{k}) = -V_{sdw}(\mathbf{k};\mathbf{p}) - 2 \int \frac{d^2q}{(2\pi)^2} V_{sdw}(\mathbf{p};\mathbf{q}) \tilde{\chi}_{\mathbf{Q},T}(\mathbf{q}) V_{sdw}(\mathbf{q};\mathbf{k}). \quad [18]$$

Here the free fermion particle-hole susceptibility is given by Eq. **14**. The leading order parameter is the eigenfunction of $\tilde{M}_{\mathbf{Q},T}(\mathbf{q},\mathbf{k}) = \tilde{\chi}_{\mathbf{Q},T}(\mathbf{q}) V_{sdw}(\mathbf{q};\mathbf{k})$ with the minimum eigenvalue. As before, we search the leading order parameter numerically after discretizing the momentum space within the energy shell.

Pseudogap of the Cuprates. Fig. 6 is generated by superposing the order parameter terms in Eq. **5** (SC), Eq. **10** (CDW), and Eq. **15** (spin density wave) to form a grand mean-field Hamiltonian. If we include all necessary components, the supervector with AF, SC, and CDW order as components will have 3 + 2 + 2 + 2 = 9 components. [The last 2 + 2 is the number of components of the CDW, associated with the $(\pm\delta, 0)$ and $(0, \pm\delta)$ order.] This large number is too complex to handle and impossible to present the results. We simplify the situation to a supervector with only three components. The first component is the superconducting order. Here we restrict the phase of the superconducting order parameter to be real. The second component is the CDW order. For this order parameter we choose the bidirectional

CDW corresponding to the in-phase superposition of the fundamental density wave in two orthogonal directions. Moreover we set the the overall (sliding) phase of the CDW order parameter to be real. The third component is the AF. Here we restrict the order parameter to a point in a particular, say the z direction. In addition to the above simplification, we also tune the magnitudes of the order parameters so that they each gives rise to an energy gap of approximately equal magnitude. This procedure leads to the following mean-field Hamiltonian:

$$H_{\mathrm{MF}} = {\sum_{\mathbf{k}}}' \sum_{s} \epsilon(\mathbf{k}) n_s(\mathbf{k}) + n_1 \left\{ \frac{1}{A} \sum_{\mathbf{p},\mathbf{k}} V_{sdw}(\mathbf{p};\mathbf{k}) \left[f_{sdw,\mathbf{Q}_s}(\mathbf{p}) \psi^{\dagger}_{\mathbf{k},c} \sigma^{z}_{cd} \psi_{\mathbf{k}+\mathbf{Q}_s,d} + f^{*}_{sdw,\mathbf{Q}_s}(\mathbf{k}) \psi^{\dagger}_{\mathbf{p}+\mathbf{Q}_s,a} \sigma^{z}_{ab} \psi_{\mathbf{p},b} \right] \right\} + n_2 \left\{ \frac{1}{A} \sum_{\mathbf{p},\mathbf{k}} \sum_{a,b} 3\epsilon_{a,b} V_{sc}(\mathbf{p};\mathbf{k}) \times \left[f_{sc}(\mathbf{p}) \psi^{\dagger}_{-\mathbf{k},a} \psi^{\dagger}_{\mathbf{k},b} + f^{*}_{sc}(\mathbf{k}) \psi_{\mathbf{p},b} \psi_{-\mathbf{p},a} \right] \right\} + n_3 \left\{ \frac{1}{A} \sum_{\mathbf{k},\mathbf{p},\mathbf{Q}_c} (-3) V_{cdw}(\mathbf{p};\mathbf{k}) \left[f_{cdw,\mathbf{Q}_c}(\mathbf{p}) \psi^{\dagger}_{\mathbf{k},a} \psi_{\mathbf{k}+\mathbf{Q}_c,a} + f^{*}_{cdw,\mathbf{Q}_c}(\mathbf{k}) \psi^{\dagger}_{\mathbf{p}+\mathbf{Q}_c,a} \psi_{\mathbf{p},a} \right] \right\}. \quad [19]$$

Here, $\mathbf{Q}_s = (\pi, \pi)$, $\mathbf{Q}_c = (\pm\delta, 0), (0, \pm\delta)$, and $f_{sdw,\mathbf{Q}_s}, f_{sc}, f_{cdw\mathbf{Q}_c}$ are the form factors of the leading order parameters determined previously, properly scaled to produce a similar maximum gap when each order parameter exists alone. The n_1, n_2, and n_3 are the components of the supervector shown in Fig. 6. In general for incommensurate δ, the above mean-field Hamiltonian couples infinite many $\mathbf{k}$ points together. The result presented previously is obtained by truncating this infinite set to the following 10-element set: $\{\mathbf{k}, \mathbf{k} \pm (\delta, 0), \mathbf{k} \pm (0, \delta), \mathbf{k} + (\pi, \pi), \mathbf{k} + (\pi, \pi) \pm (\delta, 0), \mathbf{k} + (\pi, \pi) \pm (0, \delta)\}$. This truncation leads to a 20×20 Nambu matrix for each $\mathbf{k}$. This matrix is diagonalized numerically to determine the energy gap. The minimum energy gap among all $\mathbf{k}$ (within the energy thin shell) for each direction normal to the Fermi surface is plotted in Fig. 6.

ACKNOWLEDGMENTS. We thank S. A. Kivelson for a most useful discussion on the $Q = 0$ instabilities in the cuprates. We also thank D. K. Morr, M. Norman, and S. Sachdev for helpful discussions and communications. J.C.S.D. is supported by the Center for Emergent Superconductivity, an Energy Frontier Research Center, headquartered at Brookhaven National Laboratory and funded by the US Department of Energy (DOE), under Grant DE-2009-BNL-PM015. D.-H.L. is supported by the DOE Office of Basic Energy Sciences, Division of Materials Science, under Grant DE-AC02-05CH11231.

1. Anderson PW (1995) Physics: The opening to complexity. *Proc Natl Acad Sci USA* 92(15): 6653–6654.
2. Schrieffer JR (1964) *Theory of Superconductivity* (W. A. Benjamin, New York).
3. Monthoux P, Pines D, Lonzarich GG (2007) Superconductivity without phonons. *Nature* 450(7173):1177–1183.
4. Norman MR (2011) The challenge of unconventional superconductivity. *Science* 332(6026): 196–200.
5. Scalapino DJ (2012) A common thread: The pairing interaction for unconventional superconductors. *Rev Mod Phys* 84(4):1383–1417.
6. Berg E, et al. (2009) Striped superconductors: How the cuprates intertwine spin, charge and superconducting orders. *New J Phys* 11(11):115004.
7. Fradkin E, Kivelson SA (2012) Ineluctable complexity. *Nat Phys* 8(12):864–866.
8. Orenstein J, Millis AJ (2000) Advances in the physics of high-temperature superconductivity. *Science* 288(5465):468–475.
9. Damascelli A, Hussain Z, Shen ZX (2003) Angle-resolved photoemission studies of the cuprate superconductors. *Rev Mod Phys* 75(2):473–541.
10. Norman MR and Pepin C (2003) The electronic nature of high-temperature cuprate superconductors. *Rep Prog Phys* 66(10):1547–1610.
11. Lee PA, Nagosa N, Wen X-G (2006) Physics of high-temperature superconductivity. *Rev Mod Phys* 78(1):17–85.
12. Paglione J, Greene R (2010) High-temperature superconductivity in iron-based materials. *Nat Phys* 6:645–658.
13. Wang F, Lee D-H (2011) The electron-pairing mechanism of iron-based superconductors. *Science* 332(6026):200–204.
14. Hirschfeld PJ, Korshunov MM, Mazin I (2011) Gap symmetry and structure of Fe-based superconductors. *Rep Prog Phys* 74:124508.
15. Heffner RH, Norman MR (1996) Heavy fermion superconductivity. *Comments on Condensed Matter Physics* 17(6):361–408.
16. Pfleiderer C (2009) Superconducting phases of f-electron compounds. *Rev Mod Phys* 81(4): 1551–1624.
17. Coleman P (2007) *Handbook of Magnetism and Advanced Magnetic Materials*, ed Kronmuller H, Parkin S. (John Wiley and Sons, Hoboken, NJ), Vol 1, pp 95–148.
18. Saito G, Yoshida Y (2011) Organic superconductors. *Chem Rec* 11(3):124–145.
19. Kivelson SA, et al. (2003) How to detect fluctuating stripes in the high-temperature superconductors. *Rev Mod Phys* 75(4):1201–1241.
20. Fujita M, et al. (2012) Progress in neutron scattering studies of spin excitations in high-T_c cuprates. *J Phys Soc Jpn* 81:011007.
21. Fujita K, et al. (2012) Spectroscopic imaging scanning tunneling microscopy studies of electronic structure in the superconducting and pseudogap phases of cuprate high-T_c superconductors. *J Phys Soc Jpn* 81:011005.
22. Bourges P, Sidis Y (2011) Novel magnetic order in the pseudogap state of high-T_c copper oxides superconductors. *C R Phys* 12(5-6):461–479.
23. Lawler MJ, et al. (2010) Intra-unit-cell electronic nematicity of the high-T($_c$) copper-oxide pseudogap states. *Nature* 466(7304):347–351.
24. Chuang TM, et al. (2010) Nematic electronic structure in the "parent" state of the iron-based superconductor Ca(Fe$_{(1-x)}$Co$_{(x)}$)$_2$As$_2$. *Science* 327(5962):181–184.
25. Chu JH, et al. (2010) In-plane resistivity anisotropy in an underdoped iron arsenide superconductor. *Science* 329(5993):824–826.
26. Taillefer L (2010) Scattering and pairing in cuprate superconductors. *Annu Rev Condensed Matter Phys* 1:51–70.
27. Kanoda K (1997) Electron correlation, metal-insulator transition and superconductivity in quasi-2D organic systems, (ET)(2)X. *Physica C* 282:299–302.
28. Sachdev S, La Placa R (2013) Charge ordering in metals with antiferromagnetic spin correlations. Preprint at arXiv:1303.2114v4.
29. Laughlin RB (2013) Hartree-Fock computation of the high-T_c cuprate phase diagram. Preprint at arXiv:1306.5359.
30. Monthoux P, Pines D (1993) $YBa_2Cu_3O_7$: A nearly antiferromagnetic Fermi liquid. *Phys Rev B Condens Matter* 47(10):6069–6081.
31. Sachdev S (2003) Colloquium: Order and quantum phase transitions in the cuprate superconductors. *Rev Mod Phys* 75(3):913–932.
32. Doiron-Leyraud N, et al. (2007) Quantum oscillations and the Fermi surface in an underdoped high-T_c superconductor. *Nature* 447(7144):565–568.
33. Sebastian SE, Harrison N, Lonzarich GG (2012) Towards resolution of the Fermi surface in underdoped high-T_c superconductors. *Rep Prog Phys* 75(10):102501.
34. Senthil T, Lee PA (2009) Synthesis of the phenomenology of the underdoped cuprates. *Phys Rev B* 24:245116.
35. Scalapino DJ, Loh E, Jr., Hirsch JE (1986) d -wave pairing near a spin-density-wave instability. *Phys Rev B Condens Matter* 34(11):8190–8192.
36. Gros C, Joynt R, Rice TM (1987) *Superconducting instability in the large-U limit of the two-dimensional Hubbard model.* Zeitschrift Physik B Condensed Matter 68(4):425–432.
37. Kotliar G, Liu JL (1988) Superexchange mechanism and d-wave superconductivity. *Phys Rev B Condens Matter* 38(7):5142–5145.
38. Anderson PW (1987) The Resonating Valence Bond State in La2CuO4 and Superconductivity. *Science* 235(4793):1196–1198.
39. Baskaran G, Zhou Z, Anderson PW (1987) The resonating valence bond state and high T_c superconductivity: A mean field theory. *Solid State Commun* 63(11-12):973–976.
40. Fradkin E, et al. (2010) Nematic Fermi fluids in condensed matter physics. *Annu Rev Condensed Matter Phys* 1:153–178.
41. Maharaj AV, Thomale R, Raghu D (2013) Particle-hole condensates of higher angular momentum in hexagonal systems. Preprint at arXiv:1303.2361v1.
42. Varma CM (1999) Pseudogap phase and the quantum-critical point in copper-oxide metals. *Phys Rev Lett* 83(17):3538–3541.
43. Kaminski A, et al. (2002) Spontaneous breaking of time-reversal symmetry in the pseudogap state of a high-Tc superconductor. *Nature* 416(6881):610–613.
44. Fauqué B, et al. (2006) Magnetic order in the pseudogap phase of high-T_c superconductors. *Phys Rev Lett* 96(19):197001.
45. Xia J, et al. (2008) Polar Kerr-effect measurements of the high-temperature $YBa_2Cu_3O_{6+x}$ superconductor: evidence for broken symmetry near the pseudogap temperature. *Phys Rev Lett* 100(12):127002.
46. Chang J, et al. (2012) Direct observation of competition between superconductivity and charge density wave order in $YBa_2Cu_3O_{6.67}$. *Nat Phys* 8(12):871–876.
47. Ghiringhelli G, et al. (2012) Long-range incommensurate charge fluctuations in (Y,Nd)$Ba_2Cu_3O_{(6+x)}$. *Science* 337(6096):821–825.
48. Li JX, Wu CQ, Lee D-H (2006) Checkerboard charge density wave and pseudogap in high-T_c cuprates. *Phys Rev B* 74:184515.
49. Timusk T, Statt B (1999) The pseudogap in high-temperature superconductors: An experimental survey. *Rep Prog Phys* 62(1):61–122.
50. Seo K, Bernevig BA, Hu JP (2008) Pairing symmetry in a two-orbital exchange coupling model of oxypnictides. *Phys Rev Lett* 101(20):206404.
51. Si Q, Abrahams E (2008) Strong correlations and magnetic frustration in the high Tc iron pnictides. *Phys Rev Lett* 101(7):076401.
52. Zhai H, Wang F, Lee D-H (2009) Antiferromagnetically driven electronic correlations in iron pnictides and cuprates. *Phys Rev B* 80(6):064517.
53. Zhou KJ, et al. (2013) Persistent high-energy spin excitations in iron-pnictide superconductors. *Nat Commun* 4:1470.
54. Mazin II, Singh DJ, Johannes MD, Du MH (2008) Unconventional superconductivity with a sign reversal in the order parameter of $LaFeAsO_{1-x}F_x$. *Phys Rev Lett* 101(5):057003.
55. Lynn JW, Dai P (2009) Neutron studies of the iron-based family of high Tc magnetic superconductors. *Physica C* 469(9-12):469–476.
56. Chen F, et al. (2008) Theory of electron nematic order in LaFeAsO. *Phys Rev B* 77(22):224509.
57. Xu C, Mueller M, Sachdev S (2008) Ising and spin orders in the iron-based superconductors. *Phys Rev B* 78(2):020501.
58. Yi M, et al. (2011) Symmetry-breaking orbital anisotropy observed for detwinned $Ba(Fe_{1-x}Co_x)_2$ As_2 above the spin density wave transition. *Proc Natl Acad Sci USA* 108(17):6878–6883.
59. Allan MP, et al. (2013) Imaging Cooper pairing of heavy fermions in $CeCoIn_5$. *Nat Phys* 9(8): 468–473.